

Article

The current status of the Fermilab Muon g-2 experiment

Nandita Raha ¹ on behalf of the Muon g-2 experiment

¹ INFN, Pisa

* Correspondence: nandita.raha@gmail.com

Version November 29, 2018 submitted to Journal Not Specified

Abstract: The anomalous magnetic moment of the muon can be both measured and computed to a very high precision, making it a powerful probe to test the Standard Model and search for new physics. The previous measurement by the Brookhaven E821 experiment found about three standard deviation discrepancy from the predicted value. The Muon g-2 experiment at Fermilab will improve the precision to 140 parts per billion compared to 540 parts per million of E821 by increasing statistics and using upgraded apparatus. The first run of data taking has been accomplished in Fermilab, where we already attained the statistics of E821. In this paper, I will summarize the current experimental status and briefly describe the data quality of the first run. I will compare this run with the previous E821 experiment.

Keywords: Muon; g-factor; New Physics; Calorimeters; Calibration; Gain;

1. Introduction and basic theoretical background

The magnetic moment of a muon $\vec{\mu}$ is given by,

$$\vec{\mu} = g \frac{q}{2m} \vec{s} \quad (1)$$

where \vec{s} is the intrinsic spin and g is the gyromagnetic ratio of the muon. g is predicted to be 2 in case of a structureless spin 1/2 particle of mass m and charge q , according to the Dirac theory. The muon anomaly a_μ , given by $(g-2)/2$ arises due to radiative corrections (RC), which couple the muon spin to virtual fields. These mainly include quantum electrodynamic processes (QED), electroweak loops, hadronic vacuum polarization (HVP) etc. as shown in Fig.1.

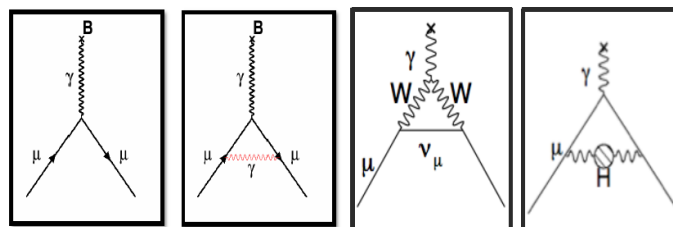


Figure 1. The SM correction in a_μ from QED, electroweak loops, HVP.

The leading RC from the lowest order QED process from the exchange of a virtual photon in Fig.1 i.e. the “Schwinger term”, is calculated to be $a_\mu = (\alpha/2\pi) = 0.00116$ [1]. The difference between experimental and theoretical values of a_μ especially at sub-ppm precision, explores new physics well above the 100 GeV scale for many Standard Model extensions [2].

In Fig.2 the yellow band represents the results of several theoretical calculations based on SM ($a_\mu = [116591802 \pm 49] \times 10^{-11}$ [3]) with a precision of 420 ppb) and the blue band represents the latest

experimental result from the previous Brookhaven E821 experiment combined with the experimental error ($a_\mu^{E821} = [116592089 \pm 63] \times 10^{-11}$ [2]) which shows a difference of 3.6σ between theory and experiment. This could indicate several possible models or any new model. These new models can be generally illustrated using a relation discussed in [4] in which new physics (N.P.) contributions scale as [5] $\delta a_\mu(N.P.) = \mathcal{O}[C(N.P.)] \times (m_\mu/M)^2$ where M is the N.P. mass scale and C is the model's coupling strength, related to any N.P. contributions to the muon mass, $C(N.P.) \equiv (\delta m_\mu(N.P.)/\delta m_\mu)$.

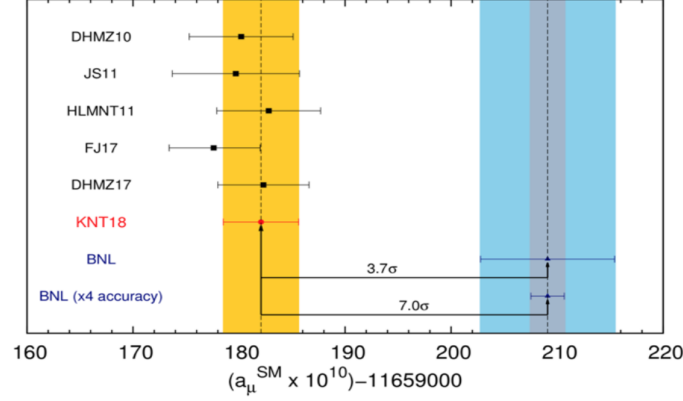


Figure 2. Comparison between theoretical and experimental results.

In the multi-TeV scale, a muon mass is generated by radiative effects. The other possible models could be due to Z' , W' , universal extra dimensions, littlest Higgs assume a typical weak-interaction scale coupling [5]. The other possibilities can represent unparticles, extra dimension models or SUSY with enhanced coupling [6]. The existence of dark photons or dark Z [7] from very weakly interacting and very light particles would correspond to a narrow band in the 10 - 100 MeV mass range, having an extremely small coupling can also be possible. Improved precision of measurement in a_μ to 140 parts per billion will continue to constrain or validate the energy scale of the models, which is the goal of "The E989 Muon g-2 Experiment". This requires 21 times more statistics than the previous Brookhaven E821 experiment and a threefold reduction of the systematic error.

2. The measurement of muon anomalous moment: The experiment

A polarized muon beam (from pion decay) having an energy of 3.09 GeV is injected (through the inflector shown in Fig.3) in a storage ring of uniform magnetic field of 1.45 T with a cyclotron frequency of ω_c . At the magic momentum of 3.09 GeV/c the muon spin precession frequency ω_s and ω_c including the Larmor and Thomas precession are approximately given by,

$$\begin{aligned}\omega_c &= \frac{e}{m\gamma}B \\ \omega_s &= \frac{e}{m\gamma}B(1 + \gamma a_\mu)\end{aligned}\tag{2}$$

We essentially measure the anomalous frequency ω_a which is ω_s relative to ω_c i.e. $\omega_a = \omega_s - \omega_c$. From the above equations this is given by,

$$\omega_a = \frac{eB}{m}a_\mu\tag{3}$$

In this experiment, we measure the muon anomaly a_μ using the following expression,

$$a_\mu = \frac{\omega_a/\omega_p}{\mu_\mu/\mu_p - \omega_a/\omega_p}\tag{4}$$

The V-A nature of the muon decay makes it a self-analyzing process to find the muon anomalous precession frequency ω_a . The maximum energy decay positrons are emitted in a preferential direction

with their momenta parallel to the muon spin. These positrons modulate with a frequency of ω_a and this frequency can thus be extracted by counting the number of positrons above an energy threshold (optimized for the best sensitivity) as a function of time. The right plot of figure 3 shows the modulated counting rate of positrons observed in the 2001 E821 data. The value of μ_μ/μ_p is taken from muonic hyperfine experiment where it is measured at ≈ 26 ppb precision [9].

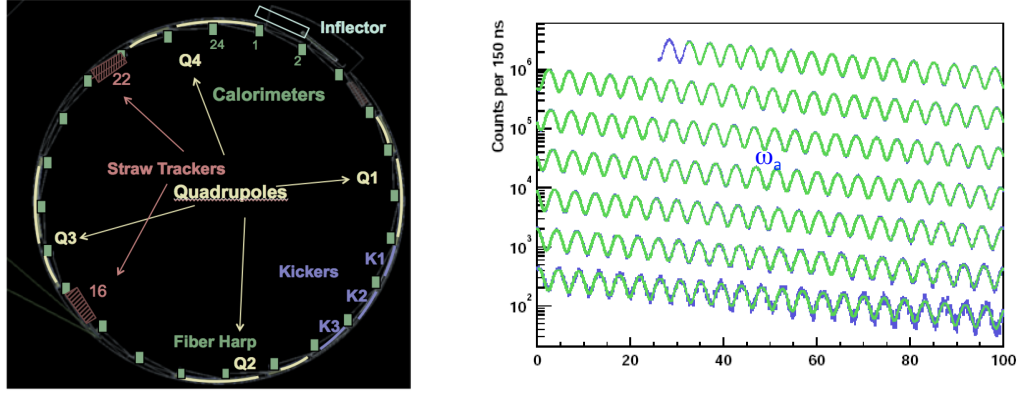


Figure 3. Left – The layout of the storage ring for the E989 experiment. Right – The modulated counting rate of the positron distribution of 2001 E821 data.

The left panel of figure 3 shows the schematic of the entire storage ring with the kickers (K1-K3), the quadrupoles (Q1-Q4), the collimators (C), the NMR trolley garage straw trackers and the fiber harps. The details of the working of each of these components will be illustrated in the subsequent sections. An electron calorimeter is placed at a position indicated by the calorimeters in green numbered (1,2,...,24). The muons decay to positrons preferentially in direction of the muon spin which are detected by the 24 calorimeters shown in Fig. 3. The time spectrum of these positrons is given by,

$$N(t) = N_0 e^{-\frac{t}{\tau}} (1 + A \cos(\omega_a t)) \quad (5)$$

from which ω_a is extracted. But care needs to be taken into account for the distortions in this spectrum due to pileup, gain instabilities, beam losses, etc.

2.1. The preparation of the Muon Beam for twenty-one times the BNL statistics

A statistical error improvement from 540 ppb to 140 ppb (21 times BNL) requires a better proton beam, better π and μ separation with an improved collection. This is accomplished by an 8 GeV proton produced in a booster which is then directed to a recycler ring further hitting an Inconel target to produce pions. Pions with an energy of 3.11 GeV are selected and transferred to a delivery ring with long decay channels (due several turns in this ring most of the pions decay before they reach the muon storage ring). This enables to produce polarized muons of energy 3.09 GeV from forward pion decays which have better spatial separated from pions and background protons. Thus, using a delivery ring eliminates background, gives a good spatial discrimination and reduces pion/proton flash. Finally, the muon bunches are transported to the muon storage ring in the Muon Campus 1 (MC1) experimental hall. An approximate run time of 18-24 months is required to acquire these statistics. To test all hardware equipment and installation of DAQ, DQM along with other software a month of the first engineering run in June 2017 took some commissioning data successfully. A production run 1 from the end of March to July 7th 2018 took place where we collected raw positron data almost twice the E821 BNL experiment. A new run 2 is scheduled to run from December 2018 to July 15th 2019.

2.2. Muon Beam – Focusing in Storage Ring

As the muon beam enters the storage ring, it experiences a magnetic field from zero strength to the maximum value of 1.45 T, which causes it to deflect. The inflector magnet cancels these fringe field effects due to the main storage ring magnet, just before the beam enters the storage ring. It has a superconducting shield so that the field generated by the inflector current does not affect the uniform field of the storage ring. A new open-ended design inflector magnet is built for E989, which prevents scattering of muons at the exit of the inflector which in turn will improve the muon storage efficiency. After exiting from the inflector, the muon beam is displaced radially by 77 mm from the ideal orbit. The three kickers direct the beam onto the orbit with the help of a pulsed vertical magnetic field which peaks at ≈ 250 G that corresponds to a kick of about ≈ 8 mrad [8]. Additionally, four electrostatic quadrupoles at 20.4 kV further enhances the radial focusing and enables the vertical focusing, but de-focuses horizontally. They are made of aluminized mylar plates and have a coverage of about $\approx 43\%$ of the circumference. The overall horizontal focussing is provided by the magnetic field. The muon beam is monitored using an Inflector Beam Monitoring System (IBMS1 and IBMS2). IBMS1 located just downstream of an initial time (T_0) counter, consists of two planes (X and Y) of 16 cylindrical scintillating fibers of 0.5 mm diameter where the X (Y)-profile fiber pitch is 5.5 (2.7) mm. This is followed by IBMS2 located inside the beam injection pipe and has a similar design as IBMS1, except that the pitch is 3.25 mm for both planes. The two planes give the X and Y profile of the beam. [10]

2.3. Further improvements and checks in the current run

A few additional detectors were installed to improve beam monitoring during kicking and scrapping phases and to investigate the effect of coherent betatron oscillations. These were mainly the fiber harps, T_0 , IBMS, and the straw trackers. The fiber harp system and the straw trackers are both needed to determine the stored muon beam distribution. In run 1 a single harp was used to study behaviour of the muon beam flux and the horizontal and vertical oscillatory effects of the beam due to an electric field at 180° near calorimeter 12 as shown in fig. 3. A couple of straw trackers are installed in the vicinity of calorimeters 16 and 22 respectively in this current run as shown in fig. 3.

2.3.1. Fiber Harps – Checking the beam in the current run

The fiber harps are strung with scintillating fibers and allow for a direct, but destructive, measurement of the distribution of stored muons and their associated beam dynamics parameters.

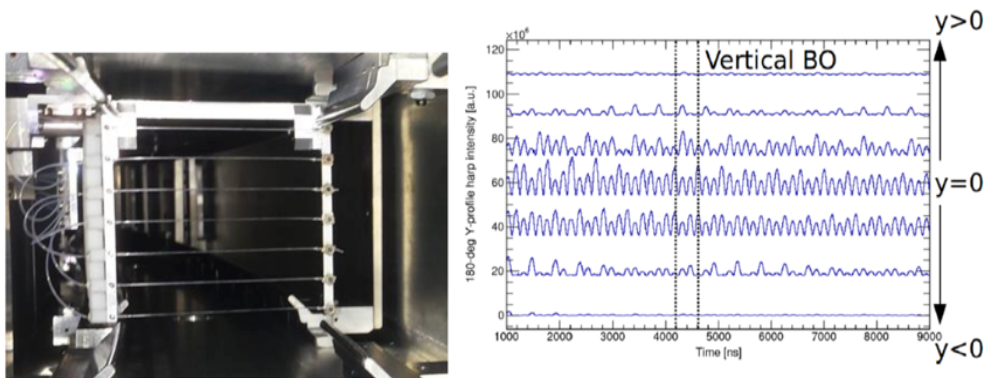


Figure 4. . The left panel is the image of a fiber harp. The right plot shows the beam profile in y direction measured by the fiber harp.

It consists of a “harp” of seven scintillating fibers of 0.5 mm diameter, each 90 mm long and separated from its neighbors by 13 mm [8]. Each scintillating fiber is further attached to a standard optical fiber as shown in the left image of figure 4. A couple of such harps were used, one suspends the fibers vertically to measure x coordinates, and the other arranges them horizontally to measure

the y coordinates. Special fiber harp runs were occasionally taken in between data taking (not during the actual data runs as it is an obstacle to the beam). The left panel of figure 4 shows the horizontal measure in y of the beam profile. Maximum oscillations are in the center of the beam (around $y=0$). This is due to the vertical component of the betatron oscillations.

2.3.2. In-Vacuum Straw Trackers

There are two straw tube trackers installed in the ring and each of them consist of 8 modules with 128 straws containing Argon-Ethane (50%) gas mixture, and having a resolution of $165\ \mu\text{m}$. Each module has two planes of straws oriented at 7.5° with respect each other, so that both the horizontal and vertical coordinates of the trajectory can be determined. The straws are made of $15\ \mu\text{m}$ thick aluminized mylar foils with a gold-plated tungsten wire ($d=25\ \mu\text{m}$) at the center.

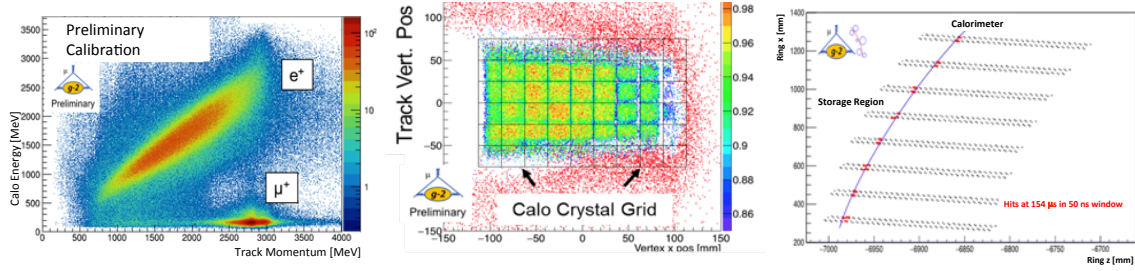


Figure 5. The left plot shows muon and positron discrimination from tracker data. The center plot shows an imaging of the calorimeters from extrapolation of positron tracks from the tracker. The right plot shows a positron hits in the tracker itself.

A forward extrapolated of the track to map with the calorimeter from the point of tangency of the ideal muon orbit allows the determination of the beam profile distribution (figure 5 right). This in turn enhances a good imaging of the calorimeters (figure 5 center). The straw trackers in combination with the calorimeters show good particle discrimination between positrons and muons based on the energy-momentum distribution (figure 5 left).

3. The Experiment – Systematic improvements

To achieve our systematic uncertainty, it is essential to reduce the systematic uncertainties in the measurement of ω_a and ω_p , which requires further improvement in equipment and other procedures related the measurement of ω_a and ω_p respectively. Systematics of 70 ppb on ω_a is achieved by using an improved laser calibration, a segmented calorimeter, better collimator in the ring, and improved tracker. Systematics of 70 ppb on ω_p is achieved by improving the uniformity and monitoring of the magnetic field, increasing accuracy of position determination of trolley, better temperature stability of the magnet, and providing active feedback to external fields [11]. We discuss these in detail in the subsequent subsections.

3.1. Systematic Improvements on ω_a

The table below shows the contribution to the systematics uncertainties of various factors on the measurement of ω_a and the proposed improvements. Here we emphasize the improvements in the calorimeters along with the laser monitoring system.

Table 1. The table shows the systematics uncertainties of various factors on the measurement of ω_a

Category	E821	E989 Improvement Plans [ppb]	Goal	Key Element [ppb]
Gain Changes	120	Better laser calibration low-energy threshold	20	Laser
Pileup	80	Low-energy samples recorded Calorimeter segmentation	40	Calo + Laser
Lost Muons	90	Better collimator in ring	20	Calo + Laser
CBO	70	Higher n value (frequency) Better match of beamline to ring	< 30	Inflector + Kicker
E and pitch	50	Improved tracker Precise storage ring simulations	30	Tracker

3.1.1. Calorimeters

The 24 calorimeters used to detect the decay positron spectrum are each made up of $54(9 \times 6)$ PbF_2 crystals (for better time and space resolution which improves pile up separation) with Silicon Photo Multipliers (better in enduring the magnetic field) and read out by custom 800 MSPS waveform digitizers.

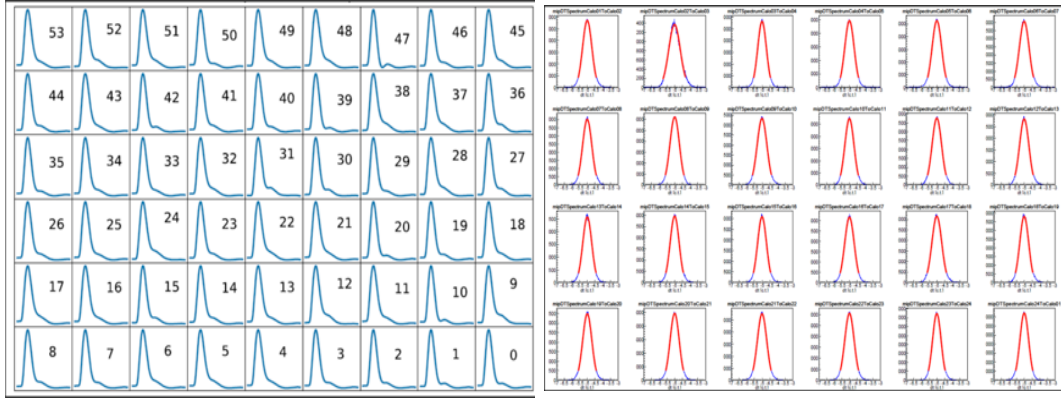


Figure 6. . The left panel shows the custom template of all 54 crystals of a calorimeter. The right shows the time distribution fitted with a Gaussian for each calorimeter.

We reconstruct the pulses read by each crystal fitting a customized pulse shape (called a template) to the actual pulses (shown in the left panel of figure 6). The time resolution of the crystals is 25 ps at 3 GeV with a pile up separation of 4.5 ns.

3.1.2. Monitoring / Calibration of Calorimeter - Laser

All the 1296 crystals of the calorimeters must be calibrated and monitored to keep uncertainties due to gain fluctuations at the sub-per mil level in the time interval corresponding to one beam fill (700 μ s) and at the sub-percent level on longer time scales. This is done using the laser calibration system. We use six laser heads (LDH-P-C-405M by PicoQuant) that provide up to 1 nJ of pulses 700 ps wide at a wavelength of 405 nm to calibrate all the calorimeters [12]. The light from each laser is divided in a ratio of 70:30 by a beam splitter. The 70% light is further divided into four equal parts and transported to the four calorimeters in the ring using 25 m-long quartz optical fibers via a diffuser (to convert the Gaussian distribution of light intensity into a more uniform and flat distribution) and a fiber bundle.

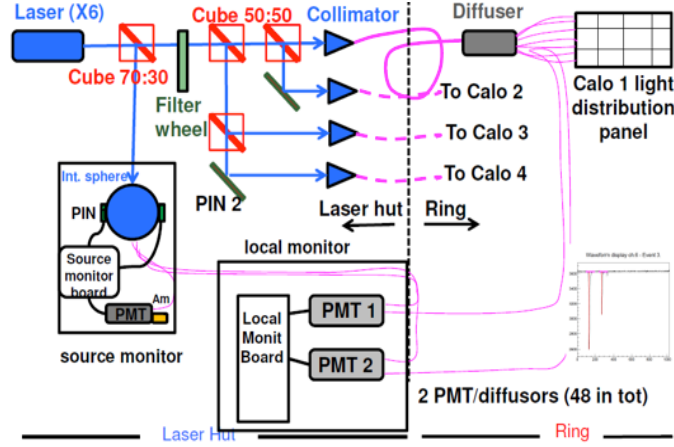


Figure 7. A schematic showing the laser calibration system.

This delivers light to each of the 54 PbF_2 crystals with the fiber bundle attached to a Delrin panel embedded with optical prisms located in front of the calorimeter. A Source Monitor (SM) is used to measure pulse-by-pulse the intensity of the remaining 30% of the laser light [13].

The optical stability of this entire system is checked using 24 Local Monitor (LM). A mini-bundle fiber transmits light from the SM to the LM. Each LM consists of a PMT which collects this light from the SM and is used as a reference signal. The light from the optical elements, the diffuser, the 25 m quartz fiber (that transmits light to the calorimeter) is transmitted back to this PMT by using a quartz fiber. Thus, the 24 LMs are used to check the stability of the light distribution chain.

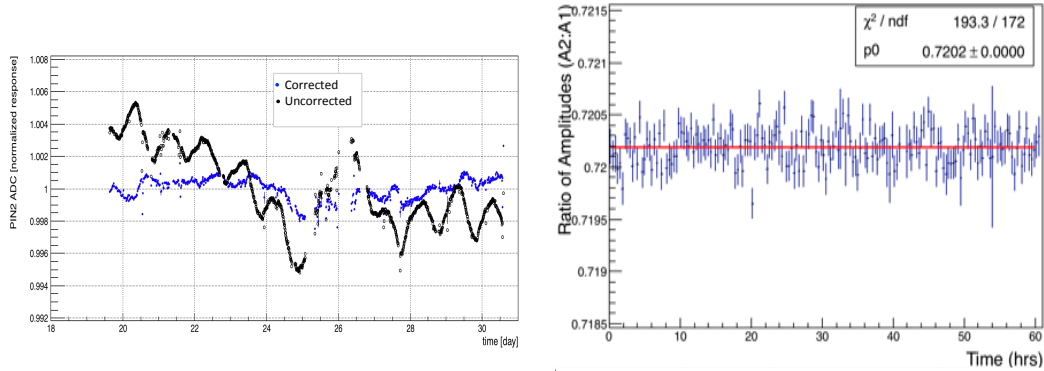


Figure 8. The stabilities of the SM (left) and LM (right) after applying a temperature correction.

Timing and gain calibrations at the subpermil level requires the system to be very stable. After applying temperature corrections, both the SM and the LM have fluctuations of the order of $\approx 10^{-4}$ (in a scale of hours) as shown in 8. This is reasonably good for the desired precision of the experiment.

3.2. Systematic Improvements on ω_p

As mentioned previously, the most important criteria for the improvement of systematics on ω_p relies primarily on the uniformity and homogeneity of the magnetic field, we briefly discuss how this was achieved in run 1 and the other upgrades related to this.

3.2.1. Magnetic Field Homogeneity / Upgrade – Current Run 1

Iron shims were used to remove asymmetries due to quadrupoles and eliminate fringe field and other stray field effects that distort the homogeneity of the main storage ring magnet. Top hats

adjustments were used above the pole pieces (outside the yoke) to change the effective dipole moment. Usage of surface correction coils and iron foils made the field more uniform. Using iron lamination in the current run further increased the uniformity of the magnetic field to 25 ppm.

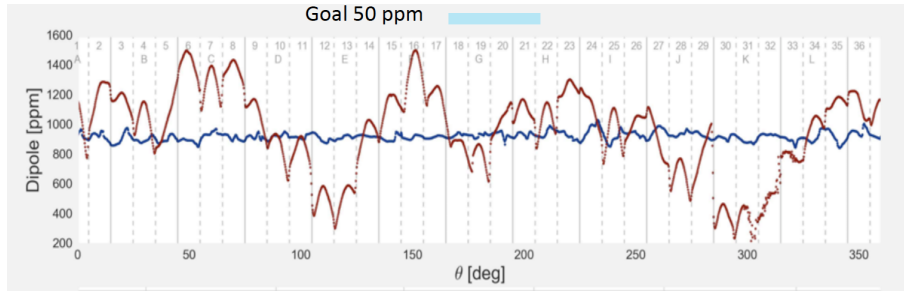


Figure 9. Comparison of the magnetic field before (brown) and after (blue) shimming, laminations, calibration etc. of the magnet.

An absolute field calibration is also essential for reducing the systematics on ω_p . A 1.45 T calibration magnet within a thermal enclosure (0.1°C) with additional probes and better electronics helped in achieving this. Trolley probe calibrations and trolley measurements of B_0 need to be done with extreme care. Plunging probes that can cross calibrate off-central probes with a better position accuracy by physical stops were used to achieve this. We used 378 fixed probes at 72 locations around the ring and more than 25 trolley calibrations run for improvements in field mapping. The results of the stability of the magnetic field due to shimming, laminations, and calibration are shown in blue in fig. 9. The brown shows the original field before these changes were applied.

4. Current run brief analysis status

Several analysis techniques using various method are underway at various places simultaneously. The two major analysis techniques we use are called the T - method and Q - method. In the T - method we use the parameterization of equation 5 with calorimeter events sorted to obtain time and energy. The events vs. time-in-fill histogram (thus the name T - method) is built from all events with reconstructed energy above a threshold energy (1.86 GeV) and ω_a is extracted by fitting this equation. All events have the same weight. Pile up protection is essential in this method. This method requires a polarization of the muon beam to be above 95% from the simulation and an asymmetry of $A = 0.38$ (refer equation 5) and number of events N_0 in the fit to be 1.6×10^{11} for a 100 ppb statistical uncertainty [8].

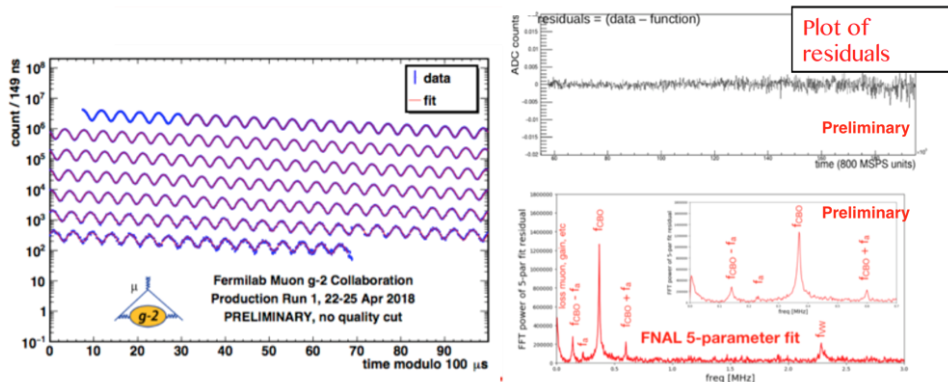


Figure 10. A fit to the modulated positron distribution plot (left). A plot of residues (top right) and a Fourier transform on this (bottom right).

In the alternative Q (charge) - method we digitize the detector current vs. time, which is proportional to the energy deposited in the calorimeter vs. time from the decay positrons. All

events are weighted inherently with energy and have an almost zero threshold. Thus, the energy in the detector will oscillate with a frequency of ω_a , which can be fitted to determine ω_a . This approach does not require pile-up protection. We perform a blind analysis in both cases with an offset (in clock frequencies and data) so that there is no bias on the analysis results. A fitted modulated positron distribution plot with T-method on a dataset of run 1 is shown in the left panel of figure 10. A plot of the residues is shown in the top right panel of figure 10. A Fourier transform on the residues plot shows structures due to CBO effects (f_{CBO}), vertical oscillations (f_{vw}), muon losses (or other effects).

5. Results and conclusion

In run 1 we were able to achieve performance improvement in beamline, injection, and detector systems compared to BNL E821. A significant improvement in systematics was also achieved as discussed before. The data quality was good enough to find a signature of ω_a , but with the current rate of positrons per fill we will achieve a factor of two lower positron events than the ideally anticipated case (as shown in the left plot of figure 11).

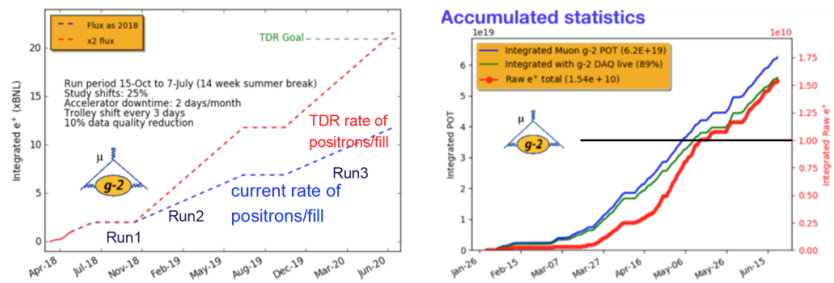


Figure 11. The left plot shows accumulated statistics of integrated positrons with a future projection. The right plot shows accumulated statistics of POT (protons on target) in blue and the raw number of positrons in red for the current run.

In this run we accumulated statistics ≈ 2 times the BNL experiment. After applying quality cuts for reconstruction of data, the accumulated statistics is the same as that of the BNL experiment. An analysis of this data is expected to be done by the second half of 2019 which will verify (or disprove) the previous result. In a few years we expect to improve the uncertainty to 140 ppb in the measurement of a_μ . If the previously measured value of a_μ is confirmed, then we can have 7σ discrepancy from SM, which will be a firm indication of physics beyond the Standard Model.

Funding: This research was funded by Istituto Nazionale di Fisica Nucleare (Italy), by Fermi Research Alliance, LLC under Contract No. DE-AC02-07CH11359 with the United States Department of Energy, and by the EU Horizon 2020 Research and Innovation Program under the Marie Skłodowska-Curie Grant Agreement No.690385 and No.734303.

References

1. J. Schwinger, *Phys. Rev.* **1948**, 73, 416.
2. G.W. Bennett, et al. *Phys. Rev. D* **73**:072003, **2006**.
3. Davier et al. *Eur. Phys. J. C* **71**, 1515, **2011**.
4. A. Czarnecki and W. J. Marciano, *Phys. Rev.*, **2001** D64, 013014
5. D. Hertzog, *Ann. Phys (Berlin)* **2015**, courtesy D. Stockinger
6. T. P. Goringe and D. W. Hertzog, **2015** doi: 10.1016/j.ppnp.2015.06.001
7. H. Davoudiasl, et al. *Phys. Rev. D* **86**, **2012** 095009
8. J. Grange, et al. Fermilab. Muon (g-2) Technical Design Report: -FN0992-E.
9. Peter Mohr, et al. *Rev. Mod. Phys.* **84**, 1527-1605, **2012**, arXiv:1203.5425 [physics.atom-ph]
10. Website: <https://gm2-docdb.fnal.gov/cgi-bin/private/ShowDocument?docid=9221>
11. W. Gohn *FERMILAB-CONF-17-602-PPD*, arXiv:1801.0008 [hep-ex]
12. A. Anastasi et al. *Nucl. Instrum. Meth. A* **842** **2017** 86.

218 13. G. Pauletta et al. *OAHOST, Volume 1, Number 1*, Article Number 5 **2017**.

219 © 2018 by the authors. Submitted to *Journal Not Specified* for possible open access
220 publication under the terms and conditions of the Creative Commons Attribution (CC BY) license
221 (<http://creativecommons.org/licenses/by/4.0/>).